Chinese Physics Letters

Air-coupled dynamic behavior of two-dimensional acoustic sensors

To cite this article before publication: Yuebin Zheng *et al* 2026 *Chinese Phys. Lett.* in press https://doi.org/10.1088/0256-307X/43/4/041001

Air-coupled dynamic behavior of two-dimensional acoustic sensors

Yuebin Zheng (郑跃滨)[1,2#], Zhaoyi Wan (万兆懿)[3#], Qin Zhou (周勤)[4#], Kaihui Liu (刘开辉)[5,3,2], Kehai Liu (刘科海)[1,2*], Chang Liu (刘畅)[3*], Enge Wang (王恩哥)[3,1*]

[1] Tsientang Institute for Advanced Study, Hangzhou, China

[2] Songshan Lake Materials Laboratory, Institute of Physics, Chinese Academy of Sciences, Dongguan, China

[3] International Centre for Quantum Materials, Collaborative Innovation Centre of Quantum Matter, Peking University, Beijing, China

[4] Shanghai Yingxin Resonance Electromechanical Technology Co., Ltd., Shanghai, China

[5] State Key Laboratory for Mesoscopic Physics, School of Physics, Peking University, Beijing, China

# These authors contributed equally to this work

* Correspondence: liu.chang@pku.edu.cn, khliu@tias.ac.cn, egwang@pku.edu.cn

High-performance acoustic devices are essential to a wide array of modern technologies, including high-sensitivity detection electronics and industrial devices. In this context, two-dimensional (2D) materials emerge as highly promising candidates for next-generation acoustic sensing, owing to their exceptional properties. However, existing models, developed primarily for conventional thick membrane materials, are inadequate as they neglect the significant air-coupled effects that dominate ultrathin 2D diaphragms. Here, we develop an equivalent lumped element model (LEM) effectively capturing the air-coupled response of graphene diaphragm down to the monolayer thickness limit. This model demonstrates a high accuracy by a maximum deviation from experiment of approximately 2.8% (~0.24 dB) in the 100-20,000 Hz range. By incorporating electrode radiation impedance, diffracted acoustic pressure, and viscous damping from backplate holes, this model enables precise optimization of 2D sensor performance. More broadly, this LEM framework can be extended to other ultrathin materials, establishing it as a general approach for modeling air-coupled dynamics in nanomaterial-based systems.

Keywords: two-dimensional materials, acoustic sensor, lumped element model, air-coupled dynamics

Highly sensitive acoustic sensors have become vital in a broad spectrum of modern technologies ranging from consumer electronics and healthcare[1-3] to industrial systems[4-6] and national defense[7, 8]. To meet the growing demand for high-performance acoustic detection, acoustic sensors need to achieve high sensitivity, which intrinsically depends on the design of transducer diaphragms with large diameters with extreme thinness[9]. This configuration enhances the diaphragm's responsivity to weak pressure variations, thus improving the sensor's ability to detect low-amplitude signals[10, 11]. However, conventional material diaphragms face fundamental limitations in achieving this configuration. One of the key bottlenecks is the severe degradation of their mechanical strength when they are fabricated into suspended structures with a large diameter to thickness ratio[12]. In this context, two-dimensional (2D) materials such as graphene provide the ideal properties of atomically thin geometry, exceptional mechanical strength, and ultra-low mass, thereby creating unprecedented opportunities for next-generation acoustic sensing platforms[13, 14].

Structurally, 2D material acoustic sensors can be categorized into unsuspended and suspended architectures. Unsuspended devices, which consist of a 2D material diaphragm on a thick substrate, such as artificial throats and eardrums[15-17] and humidity sensors[18-20], offer straightforward fabrication and excellent stability. In the thick-film model, deformation is governed primarily by bending-stiffness. This results in a displacement-dependent acoustic sensing mechanism, where the response is read out in real time by detecting the diaphragm displacement through voltage transduction[21, 22]. However, the thick substrates (e.g., polyimide or polyethylene terephthalate films) with micrometer-scale thicknesses inherently restrict their sensitivity[23].

In suspended architecture, the diaphragm is suspended without substrate support, thereby fully exhibiting the intrinsic properties of 2D materials, such as negligible bending stiffness and ultralow areal mass density (e.g., ~1×10^{-14} N·m and ~11 mg/m^2 for 5 nm-thick graphene, respectively)[24-26]. This configuration with thin diaphragm can support broadband frequency response[27]. The deformation behavior of the thin diaphragm is predominantly governed by built-in tension (also described as the prestress). Given that the density of the 2D material diaphragm is comparable to the effective mass loading of the surrounding air (~10 mg/m^2)[28-30], the air-coupled effects cannot be neglected for the dynamic response and overall performance of the 2D material sensors[31, 32].

To accurately predict the performance of the 2D material acoustic sensors, dynamic models must incorporate air-coupled effects. However, conventional models are mainly based on Wah theory[33], which only focuses on the geometric and material parameters of the diaphragms. As a result, developing a new modeling approach that accounts for these critical air-coupled interactions becomes essential. Recently, an added virtual mass increment (AVMI) model has been proposed to explain the significant deviation between theoretical predictions and experimental measurements of the resonance frequency in graphene diaphragms[13]. Nonetheless, existing modeling methods, including AVMI, still exhibit limitations in computational time and predictive accuracy (Supplementary Table S2).

In this work, we proposed an equivalent lumped-element model (LEM) specifically for 2D material acoustic sensors. While the LEM has proven effective in capturing air-damping effects in high-fidelity microphones[34, 35], they were developed for stiffness-dominated conventional diaphragms where such effects are negligible. By accounting for these critical air-coupled effects, our model achieves high predictive accuracy for the complete frequency response, as confirmed by experimental results.

Firstly, the response behaviors of thick diaphragms (Fig. 1a) and thin diaphragms (Fig. 1b) were compared by applying a simple harmonic oscillator model. Thicker diaphragms are well-suited for designing displacement-type acoustic response by tailored voltage-based readout circuits. These circuits directly detect displacement-induced changes in capacitance, arising from variations in the electrode spacing. As illustrated in the normalized frequency response of a typical thick diaphragm (Fig. 1c), the operational bandwidth is restricted to frequencies below the fundamental resonance frequency f_0, with a sharp roll-off thereafter, and confines their utility to low-frequency regimes. In contrast, thinner diaphragms are more suitable for realizing velocity-type acoustic transduction through current-based readout circuits. These circuits directly measure the average velocity of the diaphragm, which is proportional to the incident acoustic pressure variation (Fig. 1d). This design yields a flat frequency response from the fundamental resonance f_0 up to the high-frequency roll-off point f_1 (Fig. 1d), enabling the broadband detection. Their relative lower stiffness allows response of weak pressure perturbation, enhancing the overall sensitivity (Supplementary Note S1).

In order to accurately describe the acoustic sensor response, the LEM was developed in the thin diaphragm regime. The typical structure comprises a suspended 2D diaphragm positioned between two backplates. Incident waves cause the input sound pressure P_{in}. Through diffraction, pressure waves propagate around the frame (with the frame length $2L_F$) and reach the diaphragm's backside, causing the diffracted pressure P_D. The acoustic pressure radiated by the diaphragm's vibration is P_R. While P_D and P_R are treated as controllable perturbations in traditional acoustic sensors, this approximation breaks down for 2D material sensors. FEM simulations provide reliable evidence for this breakdown (detailed in Supplementary Note S3, Supplementary Table S3 and Fig. S5a). The simulated sound velocity contours clearly illustrate that the net driving force on the diaphragm emerges from the complex interplay of incident, diffracted, and radiated waves (shown in Fig. S5b), which confirms the significant contribution of air-coupled effects.

In the LEM framework, the acoustic processes of the system are represented using an electrical circuit analogy. Acoustic pressure is mapped to voltage, volume velocity (defined as the membrane velocity multiplied by the effective diaphragm area) to current, and acoustic impedance (pressure divided by volume velocity) to electrical impedance (voltage divided by current). Similar to this mapping, physical elements can be represented as electrical components. The damping element is represented by a resistor (R), the mass by an inductor (L), and the compliance element by a capacitor (C) (Fig. S4b). The incident sound force $P_{in}S$ drives the circuit through the combined influence of the radiation impedance Z_R, the characteristic impedance Z_c, the diaphragm mechanical impedance Z_m and other circuit components. A symmetrical circuit topology is applied to account for the diffracted pressure P_D, accurately describing the low-frequency air-coupled effects (detailed derivation is provided in Supplementary Note S3).

Air-coupled effects impose a pressure modulation on the membrane vibration and velocity-type frequency response, generating an added mass m_{added} that significantly affects the diaphragm's fundamental resonant frequencies, given by the following expression[13]:

$$f_{0n}=\frac{\alpha_{0n}}{2\pi a}\sqrt{\frac{T}{\mu+m_{added}/S}} \tag{1}$$

where n denotes the mode index, α_{0n} are Bessel zeros (e.g., 2.405 for n=1), T is the diaphragm tension, S is the effective area of the diaphragm and μ is the areal mass density of the diaphragm. The added mass m_{added} effectively increases the total inertial load of the diaphragm, resulting in a pronounced downward shift in f_{01} (blue solid line in Fig. 2b) compared to the vacuum simulation (black dotted line in Fig. 2b). Furthermore, the coupling effects from P_{D} and P_{R} effectively suppress the resonant peak and flatten the frequency response of the sensor (blue solid line in Fig. 2b). These effects are further substantiated by experimental measurements (Fig. 2c). Specifically, the fundamental resonant frequencies of graphene/graphite diaphragms with thicknesses spanning 1 nm to 200 nm are calculated using the LEM (blue solid line in Fig. 2c), Wah theory (gray dashed line in Fig. 2c), COMSOL FEM simulations (cyan circles in Fig. 2c), and directly compared to the experimental data (pink rectangles in Fig. 2c; detailed parameters in Supplementary Table S3). These comprehensive comparisons clearly demonstrate that the LEM delivers the highest predictive accuracy across the entire thickness range. Notably, under identical conditions, the LEM not only delivers similar precision compared to FEM, but does so in substantially reduced computational time (approximately seconds for LEM versus minutes for FEM).

To fully capture the complete structure of the 2D material-based acoustic sensor, the proposed LEM framework is extended and refined (Fig. 3a). This further incorporates two perforated backplates with arrays of small holes (diameter a_{h}) separated by air gaps of thickness g on each side. The hole dimensions are maintained much smaller than the operating acoustic wavelength to ensure the validity of the lumped-element approximations. The dual-backplate configuration is deliberately chosen to enable the diaphragm to operate in a highly linear regime while retaining exceptional sensitivity[27]. Conventionally the small holes act as acoustic conduits. However, due to the significant air-related mutual coupling between adjacent holes, a more accurate description of the effective radiation impedance Z_{e} of the entire backplate is required. To quantify this behavior, we introduce a filling factor Γ to represent the fractional open area of the holes on each backplate. Viscous and thermal losses through the holes are fully incorporated into the comprehensive air-coupling framework. These dissipative effects profoundly influence both the back pressure P_{B} behind the diaphragm and the backplate radiation pressure P_{e} from the perforated backplates, ensuring an accurate and complete description of the 2D material sensor behavior (detailed in Supplementary Note S4).

Integrating all the air-coupled interactions, we derive a complete equivalent LEM tailored for audio-frequency graphene-based acoustic sensors (Fig. 3b, with the geometrical parameters detailed in Supplementary Table S5). To elucidate how these air-coupled effects modulate the real acoustic sensor response, we first examine the effective net driving force $\Delta F=S(P_{in}-P_B)$ acting on the diaphragm (Fig. 4a). Due to pronounced diffraction at low frequencies, the opposing back pressure P_B effectively counteracts the incident pressure P_{in}, resulting in a markedly diminished real part of the effective driving force in the low-frequency regime (red dashed line in Fig. 4a). Physically, this manifests as a drastic reduction in the net force on the diaphragm, which directly accounts for the characteristic roll-off and flattening of the sensor's frequency response at low frequencies. To demonstrate that this flattening of the frequency response stems directly from the back pressure P_B, we compare model predictions with and without its inclusion (Fig. 4b). The presence of P_B dramatically suppresses both the diaphragm's vibration velocity (membrane velocity) and the resonance peak amplitude (red dashed line in Fig. 4b). In contrast, neglecting P_B produces an unrealistic upturn in the response, which contradicts the established behavior of 2D material acoustic sensors. This profound influence of P_B further emphasizes the necessity of incorporating air-coupling effects in accurate modeling of the 2D material acoustic sensors.

More importantly, the LEM enables direct optimization of acoustic damping and losses that are challenging to precisely control in other models. By intuitively mapping these acoustic damping and loss mechanisms to specific elements in the electro-acoustic equivalent circuit, the model enables optimization not only through adjustments to geometric parameters (e.g., the backplate filling factor Γ), but also by directly assigning values to abstract impedance and damping components. By tuning the backplate filling factor (Fig. 4c), the damping mechanisms driven by viscous and thermal losses can be quantitatively controlled. A higher Γ (increased open area fraction) significantly amplifies fundamental vibration amplitudes which can be designed for sensors targeting low-frequency performance. Conversely, a lower Γ enhances resonance damping, resulting in an extended flat bandwidth more suited for broadband acoustic sensing applications. Increasing the radius (Fig. 4d) or decreasing the thickness (Fig. 4e) shifts resonance peaks toward lower frequencies. It is notable that, for thinner membranes, air damping effectively suppresses higher-order resonance modes, leading to a smoother, flatter broadband response (Fig. S8). At monolayer limit (~0.34 nm), for example, a 20 mm diameter diaphragm

under 1 MPa prestress can achieve a resonance frequency of ~6 Hz, yielding a simulated frequency response wider and flatter compared to those obtained with thicker diaphragms. Furthermore, the velocity-type frequency response predicted by the equivalent LEM is rigorously validated against experimental measurements (Fig. 4f). The model achieves high agreement with the data, exhibiting a maximum deviation of only ~2.8% (~0.24 dB) across the 100-20,000 Hz audio range.

Leveraging the LEM for design optimization, the fabricated device realizes an extraordinary diameter to thickness ratio approaching 10^6 (80 mm diameter and 100 nm thickness; Fig. S2b). This achieves a flat bandwidth exceeding 30 kHz, with the sensitivity approaching the highest values for capacitive acoustic sensors. These results demonstrate the practical utility of the LEM as a powerful tool for engineering high-performance acoustic sensors. The LEM can also be extended for high-frequency and large-radiation applications (Fig. S6b), making it suitable for aeroacoustic or ultrasonic transduction, such as micro-electro-mechanical systems (MEMS) and nano-electro-mechanical systems (NEMS) resonators[36].

In conclusion, the developed equivalent LEM provides a highly accurate framework for modeling air-coupled dynamics in suspended 2D material acoustic sensors. By mapping physical quantities to specific elements in the electro-acoustic equivalent circuit, the LEM enables direct prediction and parameter control. This versatile framework holds substantial promise for extension to the vibration dynamics of other air-coupled nanostructures, offering valuable guidance and inspiration for future research and device engineering.

Reference

1. Wang Y, Sun C, and Ahmed D 2025 *Nat. Electron.* **8** 485–495
2. Chen Y, Liu H, Reilly M, Bae H, and Yu M 2014 *Nat. Commun.* **5** 5247
3. Wu Z, Liu K, Wang Y, and Zheng Y 2015 *J. Intell. Mater. Syst. Struct.* **26** 2181–2195
4. Zheng Y, Liu K, Wu Z, Gao D, Gorgin R, Ma S, and Lei Z 2019 *Ultrasonics* **92** 13–20
5. Basiri-Esfahani S, Armin A, Forstner S, and Bowen W P 2019 *Nat. Commun.* **10** 132
6. Cheng X, Zhou X, Huang C, Liu C, Ma C J, Hong H, Yu W T, Liu K H, and Liu Z F 2021 *Chin. Phys. B* **30** 118103
7. Kaushik B, Nance D, and Ahuja K 2005 *AIAA/CEAS Aeroacoustics Conference* 2005-2997
8. de Bree H E and Wind J W 2011 *Proc. SPIE* **8047** 80470C
9. Wan Z Y, Liu H Z, Zheng Y B, Ma Y H, Liu K H, Zhou X, Liu C, Liu K H, and Wang E 2024 *Adv. Funct. Mater.* **34** 2303519
10. Pan L, Chortos A, Yu G, Wang Y, Isaacson S, Allen R, Shi Y, Dauskardt R, and Bao Z 2014 *Nat. Commun.* **5** 3002
11. Zhu J K, Wang L M, Wu J Q, Liang Y C, Xiao F, Xu B, Zhang Z J, Fan X L, Zhou Y, and Xia J 2023 *Chin. Phys. Lett.* **40** 038102
12. Beranek L L and Mellow T J 2019 *Acoustics: Sound Fields, Transducers and Vibration* (Academic Press)
13. Pezone R, Baglioni G, van Ruiten C, Anzinger S, Wasisto H S, Sarro P M, Steeneken P G, and Vollebregt S 2024 *Appl. Phys. Lett.* **124** 123503
14. Yang Y B, Wang R Z, and Wang C H 2023 *Nanoscale* **15** 1860–1868
15. Dagdeviren C, Su Y, Joe P, Yona R, Liu Y, Kim Y S, Huang Y A, Damadoran A R, Xia J, Martin L W, Huang Y G, and Rogers J A 2014 *Nat. Commun.* **5** 4496
16. Pozo-Bayón M Á, Santos M, Martín-Álvarez P J, and Reineccius G A 2009 *Flavour Fragr. J.* **24** 226–233
17. Yang J, Chen J, Su Y, Jing Q, Li Z, Yi F, Wen X, Wang Z, and Wang Z L 2015 *Adv. Mater.* **27** 1316–1326
18. Smith A D, Elgammal K, Niklaus F, Delin A, Fischer A C, Vaziri S, Forsberg F, Råsander M, Hugosson H W, Bergqvist L, Schröder S, Kataria S, Östling M, and Lemme M C 2015 *Nanoscale* **7** 19099–19109
19. Santra S, Hu G, Howe R C T, De Luca A, Ali S Z, Udrea F, Gardner J W, Ray S K, Guha P K, and Hasan T 2015 *Sci. Rep.* **5** 17374
20. Bi H, Yin K, Xie X, Ji J, Wan S, Sun L T, Terrones M, and Dresselhaus M S 2013 *Sci. Rep.* **3** 2714
21. Jabareen M and Eisenberger M 2001 *J. Sound Vib.* **240** 409–429

22. Kirchhoff G 1850 *J. Reine Angew. Math.* **40** 51–88

23. Gou G Y, Li X S, Jian J M, Tian H, Wu F, Ren J, Geng X S, Xu J D, Qiao Y C, Yan Z Y, Dun G H, Ahn C W, Yang Y, and Ren T L 2022 *Sci. Adv.* **8** eabn2156

24. Lee J U, Yoon D, and Cheong H 2012 *Nano Lett.* **12** 4444–4448

25. Gorgolis G and Galiotis C 2017 *2D Mater.* **4** 032001

26. Lee J, Wang Z, He K, Shan J, and Feng P X L 2013 *ACS Nano* **7** 6086–6091

27. Zhou Q, Zheng J, Onishi S, Crommie M F, and Zettl A K 2015 *Proc. Natl. Acad. Sci. U.S.A.* **112** 8942–8946

28. Kinsler L E, Frey A R, Coppens A B, and Sanders J V 2000 *Fundamentals of Acoustics* (John Wiley & Sons)

29. Li S and Li X 2008 *Appl. Acoust.* **69** 272–279

30. Beranek L L and Mellow T J 2012 *Acoustics: Sound Fields and Transducers* (Academic Press)

31. Nagaya K 1978 *J. Appl. Mech.* **45** 153–158

32. Chiang H Y and Huang Y H 2018 *Appl. Acoust.* **129** 365–378

33. Wah T 1962 *J. Acoust. Soc. Am.* **34** 275–281

34. Liu H, Olson D A, and Yu M 2014 *J. Sound Vib.* **333** 7051–7075

35. Guan X 2025 *Sci. Rep.* **15** 27434

36. Lin S C, Tian T, Yin P R, Huang P, Zhang L, and Du J F 2021 *Chin. Phys. Lett.* **38** 020502

Acknowledgements: This work was supported by the Guangdong Major Project of Basic and Applied Basic Research (grant numbers 2021B0301030002); the New Cornerstone Science Foundation through the XPLORER PRIZE; the National Natural Science Foundation of China (grant numbers 12574185); Postdoctoral Science Foundation of China (grant numbers 2022M720629, 2025T180922, 2022M710232); Hangzhou Tsientang Education Foundation; and Young Elite Scientists Sponsorship Program of the Beijing High Innovation Plan.

Author contributions: Y.Z., Z.W. and Q.Z. contributed equally to this work. K.L. (Kaihui), K.L. (Kehai), C.L. and E.W. supervised the project. Q.Z. conceptualized the study and performed formal analysis. Y.Z. and Z.W. developed the methodology. Y.Z. developed the software and modeling. Z.W. performed validation. Y.Z. and Q.Z. prepared the original draft. Z.W., C.L., K.L. (Kehai), K.L. (Kaihui) and E.W. reviewed and edited the manuscript. All authors discussed the results and contributed to the final paper.

Competing interests: The authors declare no competing interests.

Methods:

Finite element simulations. Dynamic simulations were performed using COMSOL Multiphysics software, coupling the structural mechanics and pressure acoustics modules to model bidirectional fluid-structure interactions. The suspended graphene/graphite diaphragm was defined with prestress (1-8 MPa), Young's modulus (1 TPa), Poisson's ratio (0.17), and density (2200 kg/m^3), with thickness varying from monolayer (~0.34 nm) to 200 nm and diameter up to 100 mm. A 1 Pa plane-wave background pressure field was applied as incident excitation. The rigid frame and perforated backplates were modeled with appropriate boundary conditions, incorporating air gaps (0.35 mm), electrode thickness (0.2 mm), and hole arrays. Air properties included density (1.225 kg/m^3) and sound speed (340 m/s). Radiation boundaries simulated open-space conditions, while frequency-domain studies swept 20 Hz-100 kHz to compute velocity responses, resonance frequencies, and air-coupled effects (radiation impedance, diffracted back pressure, and viscous damping). Mesh refinement ensured convergence at multi-physical interfaces.

Device Fabrication and Characterization. The 2D material acoustic sensors were fabricated by spin-coating graphene oxide (GO) dispersion (2-10 mg/mL, diluted from commercial GO slurry

(Hangzhou Gaoxi Technology)) onto oxygen plasma-treated silicon substrates to form multilayer films (~100 nm thick), followed by chemical reduction in concentrated hydroiodic acid (HI, Shanghai Macklin Biochemical Technology). The reduced rGO films were detached, floated on deionized water containing ~0.01 wt% sodium dodecyl sulfate (SDS, Shanghai Macklin Biochemical Technology) to reduce surface tension, scooped onto 304 stainless steel rings, dried, and tensioned via vacuum-assisted transfer to rigid frames (diameter up to 80 mm). Polypropylene insulating spacers (~0.3 mm thick) and perforated backplates (Cu 2680, 0.2 mm thick, hole diameter ~0.4-0.85 mm, filling factor ~0.4) were assembled to form dual-backplate capacitive structures with ~0.125-0.35 mm air gaps, with electrical connections via conductive adhesive and encapsulation in glass-fiber-reinforced polycarbonate housing. Initial capacitance was ~350 pF, measured using an LCR meter (HIOKI IM3536). Acoustic characterization was performed in a custom anechoic chamber under free-field conditions. The prototype and a calibrated reference microphone were co-aligned on the acoustic axis. Swept-sine frequency response (100 Hz-100 kHz) was measured in two segments using segmented loudspeakers (YAMAHA HS8 for 100 Hz-20 kHz; Avisoft-UltraSoundGate 116Hme ultrasound speaker for 20 kHz-100 kHz), with signals recorded via a multi-channel acquisition system and analyzed using FFT. Field uniformity was calibrated to ± 1 dB through closed-loop reference compensation.

Figures and captions

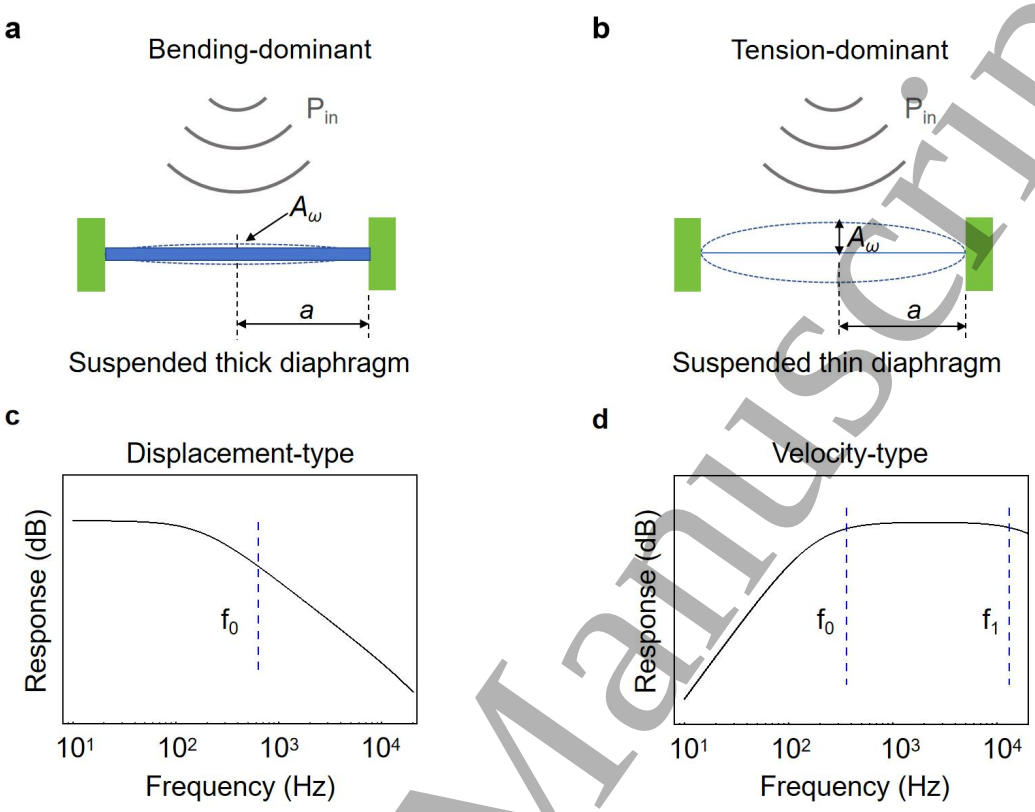

Fig. 1 | Comparison of suspended architectures in 2D material acoustic sensors and their representative frequency responses. a, Schematic of the suspended thick diaphragm configuration in acoustic process, showing that the incident sound pressure P_{in} acts on the diaphragm. The diaphragm has radius a. The diaphragm's deflection A_ω is governed by thin-plate theory for relatively thick films, where bending stiffness dominates vibrational deformation. **b,** Schematic of the suspended thin diaphragm configuration, made from 2D materials and governed by thin-membrane vibration theory, where prestress dominates deflection and damping effects are prominent, in which prestress dominates the deflection behavior and damping effects become prominent. **c,** Displacement-type frequency response of unsuspended devices, by designing voltage transduction readout circuit, showing a stable operating bandwidth limited to sub-resonant frequencies below the fundamental resonance frequency f_0. **d,** Velocity-type frequency response of suspended devices, by designing current transduction readout circuit, exhibiting an extended flat bandwidth from the fundamental resonance frequency f_0 up to the high-frequency roll-off frequency f_1.

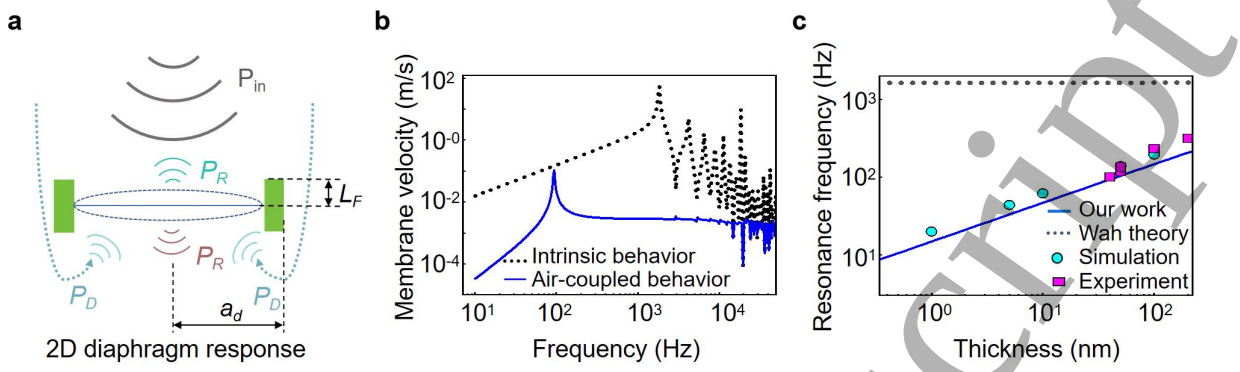

Fig. 2 | Velocity-type frequency responses and comparative modeling analysis for graphene-based 2D material diaphragms. a, Schematic of the acoustic response process in a 2D material acoustic sensor, showing incident sound pressure P_{in} diffracting around the rigid frame to generate diffracted sound pressure P_D on the diaphragm and outer frame. The diaphragm's vibration produces radiation pressure P_R, illustrating air-coupling effects at low frequencies. The rigid frame has half-length L_F, and the outer frame has radius a_d. **b,** Velocity-type frequency responses of the graphene diaphragm under vacuum (black dotted line) and air-coupled (blue solid line) conditions. The marked downward shift in resonance frequencies under air-coupled conditions arises primarily from the added mass effect due to acoustic radiation impedance. **c,** Comparison of predicted and measured fundamental resonance frequencies (f_0) for graphene-based 2D material diaphragms with thicknesses ranging from 1 nm to 200 nm. Predictions are shown for the proposed LEM (blue solid line), Wah theory (gray dashed line), COMSOL simulations (cyan circles), and experimental data (pink rectangles). Wah theory substantially overestimates f_0 in the sub-200 nm regime owing to its neglect of air-coupled damping. In contrast, the LEM yields the closest agreement with both simulations and experiments, confirming its superior accuracy in capturing air-diaphragm interactions in ultrathin diaphragms.

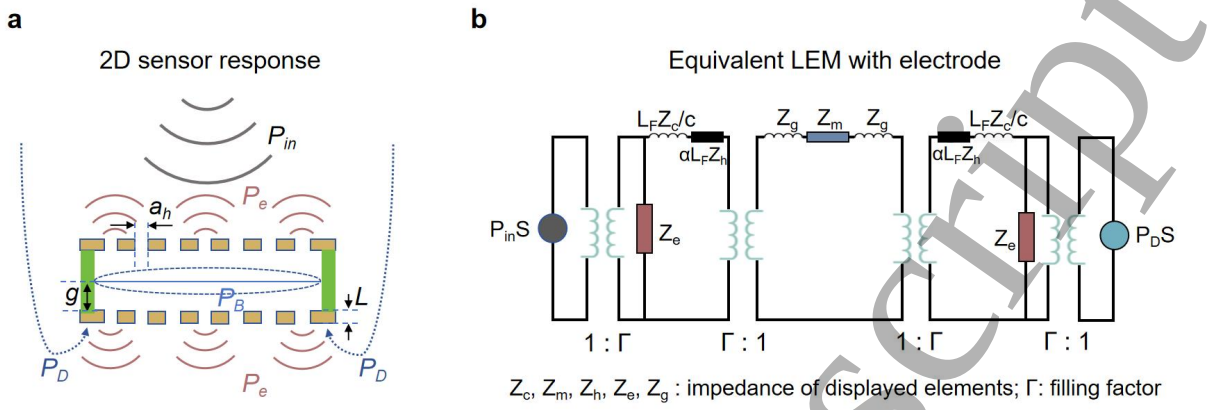

Fig. 3 | Schematic of the 2D material-based acoustic sensor structure and its equivalent lumped-element models (LEMs). a, Cross-sectional view of the sensor architecture. Incident acoustic pressure P_{in} arrives from the top, diffracts around the rigid frame to produce diffracted pressure P_D, and drives diaphragm vibration to generate backplate radiated pressure P_e from the perforated back electrodes. The opposing pressure on the backside is P_B. Key geometrical parameters include air gap thickness g, electrode thickness L, hole radius a_h, and the membrane effective surface area S (with radius a). The perforated backplates feature arrays of small holes that facilitate acoustic transmission and damping. **b,** Complete equivalent LEM incorporating perforated backplate effects. The circuit uses $P_{in}S$ as the source, connected through Z_c (scaled by L/c) and a 1:Γ transformer (where Γ is the filling factor representing the open hole area fraction), then to hole impedance Z_h (scaled by $\alpha L/Z_h$, with α as the attenuation coefficient), electrode radiation impedance Z_e, and transformed impedance across the gap Z_g, paralleled with Z_m, and symmetrically mirrored on the backside leading to P_DS. Additional transformers (1:Γ and Γ:1) account for area discontinuities and mutual hole interactions.

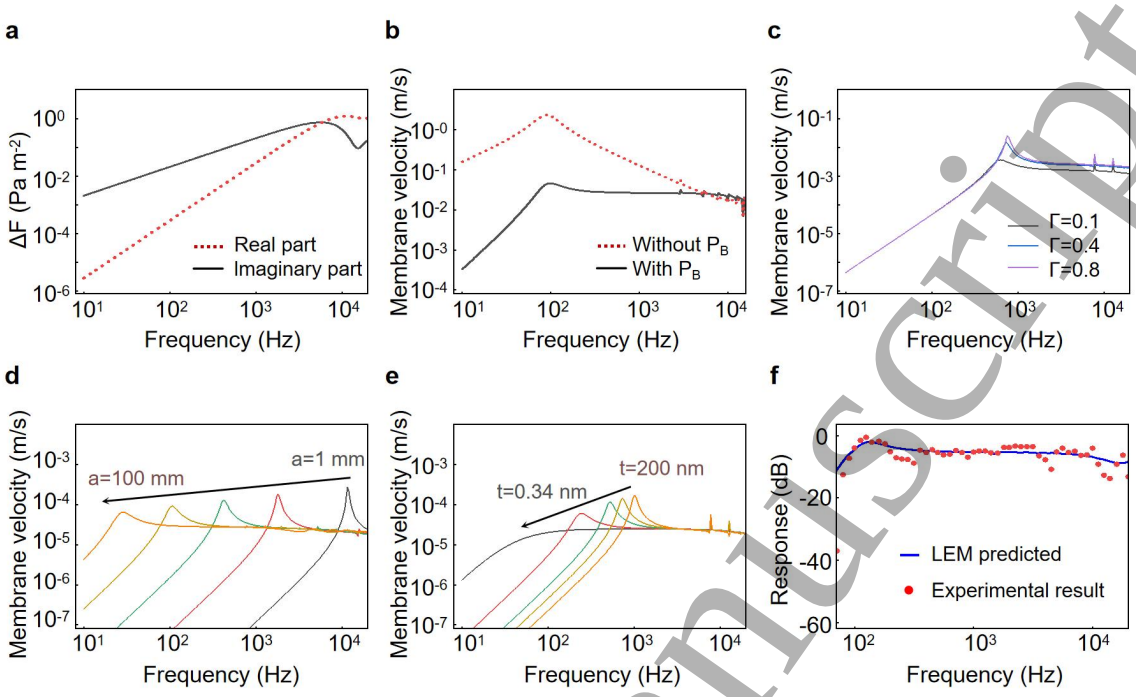

Fig. 4 | Dynamic response characteristics, parameter optimization, and experimental validation of the equivalent LEM for graphene-based acoustic sensors. a, Frequency dependence of the effective driving force on the diaphragm, decomposed into real (in-phase) and imaginary (quadrature) components. In the low-frequency regime, the markedly diminished real part reflects strong opposition from back pressure P_B, resulting in reduced net drive and suppression of resonance peaks. **b,** Velocity-frequency responses with (black solid line) and without (red dotted line) inclusion of back pressure P_B, illustrating that P_B is essential for reproducing the characteristic low-frequency roll-off and flattened bandwidth observed in ultrathin diaphragms. **c,** Velocity-frequency responses as a function of backplate filling factor Γ. Tuning Γ enables precise control of viscous and thermal damping, optimizing low-frequency response and resonance behavior. **d,** Velocity-frequency responses for diaphragms of varying radius (diameters from 1 mm to 100 mm, at fixed thickness of 20 nm and Γ=0.4) (calculated). Increasing radius shifts resonance peaks to lower frequencies, broadening and flattening the response. **e,** Velocity-frequency responses for diaphragms of varying thickness (200 nm to 0.34 nm monolayer, at fixed diameter of 20 mm and Γ=0.4). Decreasing thickness similarly lowers resonance frequencies while extending and flattening the bandwidth. The results of Fig. 4a-e were calculated by using the proposed LEM framework. **f,** Comparison of LEM-predicted (blue line; calculated) and experimentally measured (red dots) velocity-frequency responses for a fabricated graphite diaphragm sensor. The model shows excellent agreement across the audio range, with a maximum deviation of only ~2.8% (~0.24 dB).